Available online at www.sciencedirect.com
SCIENCE DIRECT®
Journal of Power Sources 119–121 (2003) 232–238
JOURNAL OF POWER SOURCES
www.elsevier.com/locate/jpowsour

Olivine-type cathodes Achievements and problems

Atsuo Yamada[a,*], Mamoru Hosoya[a], Sai-Cheong Chung[a], Yoshihiro Kudo[b], Koichiro Hinokuma[a], Kuang-Yu Liu[b], Yoshio Nishi[a]

[a]*Materials Laboratories, Sony Corporation, 2-1-1 Shinsakuragaoka, Hodogaya, Yokohama 240-0036, Japan*
[b]*Technical Solution Center, Sony Corporation, 4-16-1 Okada, Atsugi 243-0021, Japan*

Abstract

The recent progress at Sony in the design of practical olivine-type cathodes is reviewed briefly. First principle calculations revealed $LiFePO_4$ is a semiconductor with ca. 0.3 eV band gap and $LiMnPO_4$ is an insulator with ca. 2 eV band gap, which seems the major intrinsic obstacle to a smooth redox reaction at 4 V in the Mn-rich phase. Attention is also focused on the lattice frustration induced by the strong electron (Mn^{3+}: $3d^4$–$e_g\sigma^*$)–lattice interaction (Jahn-Teller effect) in the charged state of $Li(Mn_yFe_{1-y})PO_4$ ($0 \leq y \leq 1$). Dense nanocomposite formation with disordered conductive carbon as well as the choice of the appropriate synthetic precursors is highlighted as important engineering aspects, followed by some specific issues concerning tolerance to unusual conditions.

Keywords: Olivine; Cathode; Iron; Phosphate; Lithium; Battery

1. Introduction

Since the demonstration of reversible electrochemical lithium insertion–extraction for $LiFePO_4$ in 1997 [1], lithium transition metal phosphates with ordered-olivine structures, $LiMPO_4$ (M = Co, Ni, Mn, Fe, Cu), have attracted much attention as promising new cathode materials for rechargeable lithium batteries [3–34]. Crystalline $LiMPO_4$ has an orthorhombic unit cell (D_{2h}^{16}—space group *Pmnb*), which accommodates four units of $LiMPO_4$. In phospho-olivines, all of the oxygen ions form strong covalent bonds with P^{5+} to form the PO_4^{3-} tetrahedral polyanion and stabilize the entire three-dimensional framework. This guarantees stable operation at higher temperatures [7,8] and extreme safety under abusive conditions [1,3,7,8,25,33], which adds greatly to the attractiveness of the olivine-type cathode. The P_{tet}–O–M_{oct} linkage in the structure induces the superexchange interaction that tunes the M^{3+}/M^{2+} redox energy to useful levels (3.4, 4.1, and 4.8 V for Fe^{3+}/Fe^{2+}, Mn^{3+}/Mn^{2+}, and Co^{3+}/Co^{2+}, respectively) [1,18], which is called the ''inductive effect''. The positions of the redox couples were also confirmed by the first principle calculations in our laboratory [3]. Their theoretical capacity of up to 170 mAh/g provides high energy density compared to that of $LiCoO_2$, stabilized $LiNiO_2$, and $LiMn_2O_4$ [3]. In the olivine-type $LiMPO_4$ family, $LiFePO_4$, $LiMnPO_4$, and their solid solution system, $Li(Mn_yFe_{1-y})PO_4$ [1,4–6], look promising because they operate at 3.4–4.1 V versus Li/Li^+. This is providential because it is not so high as to decompose the organic electrolyte but it is not so low as to sacrifice energy density.

It has been shown, however, that the sufficient capacity and kinetics at 4.1 V are not possible without Fe co-existing with Mn at the octahedral 4c site [1]. Padhi et al. have performed experiments on the electrochemical charge and discharge characteristics of $Li(Mn_y^{2+}Fe_{1-y}^{2+})PO_4$ (y = 0.25, 0.50, 0.75, 1.0) and reported that the width of the 4.1 V plateau (Mn^{3+}/Mn^{2+}) relative to that of the 3.4 V plateau (Fe^{3+}/Fe^{2+}) increases as the Mn content y is increased. However, the total capacity decreases rapidly at $y > 0.8$ due to an abrupt increase in the polarization [1]. In addition, it should be noted that there are two intrinsic negative aspects of olivine-type materials for lithium battery cathodes: (1) the lower true density ($LiMnPO_4$: 3.4 g/cm^3; $LiFePO_4$: 3.6 g/cm^3; $LiMn_2O_4$: 4.2 g/cm^3; $LiNiO_2$: 4.8 g/cm^3; $LiCoO_2$: 5.1 g/cm^3) [3,17]; and (2)

* Corresponding author. Present address: Department of Electronic Chemistry, Tokyo Institute of Technology, 4259 Nagatsuta, Midori, Yokohama 226-8502, Japan.
E-mail address: yamada@echem.titech.ac.jp (A. Yamada).

0378-7753/03/$ – see front matter
doi:10.1016/S0378-7753(03)00239-8

the much lower electronic conductivity, particularly in the Mn-rich phase [4].

In this short review article, a selection of important scientific and engineering originals is summarized with respect to the development of olivine-type cathodes at Sony during 1994–1999 [2–14]. Systematic representations are made of the electron transport, crystal chemistry, and the phase diagram of $Li_x(Mn_yFe_{1-y})PO_4$ to explain the difficulty of using the Mn-rich phase as a practical lithium battery cathode. We also demonstrate our original technical solutions to overcome the material's intrinsic problems as well as the promising perspectives for the future scale-up production. Finally, emphasis is given to the impressive stability to some of the unusual conditions to which consumer batteries may be exposed.

2. Methodology

Ab initio calculations were applied to the electronic structures of the cathodes [3,4]. All calculations were done within the density functional theory approximation using the gradient corrected functional for exchange and correlation. The FP-LAPW code Wien97 was used.

The olivine phase was synthesized by solid-state reactions in purified N_2 gas flow at 600 °C, as reported in previous publications [3–6]. For electrochemical tests, nanocomposites with disordered conductive carbon were formed during the sintering process [7–10], as will be described later. Chemical oxidation to obtain the desired compositions in $Li_x(Mn_yFe_{1-y})PO_4$ was performed by reacting $Li(Mn_yFe_{1-y})PO_4$ with nitronium tetrafluoroborate (NO_2BF_4) in acetonitrile to produce $(Mn_yFe_{1-y})PO_4$, followed by chemical lithiation with LiI in acetonitrile [4–6]. X-ray powder diffraction, ^{57}Fe Mössbauer spectra, X-ray absorption spectroscopy, and inductively coupled plasma spectroscopy were used for materials characterization.

The performance of the $Li(Mn_yFe_{1-y})PO_4$ cathodes was evaluated using a coin-type cell (size 2025) with a lithium metal anode. The cathode was a homogeneous composite of $Li(Mn_yFe_{1-y})PO_4$/carbon black/polyvinylidene fluoride (PVDF) with weight ratio ca. 90:8:2 (60 mg of total weight), and the electrolyte was a 1 M $LiPF_6$–propylene carbonate/dimethyl carbonate (PC/DMC) solution.

3. Results and discussion

3.1. Electronic structure [4]

The total density of states (DOS) for $LiFePO_4$ and $LiMnPO_4$ are shown in Fig. 1. The narrow bands near the Fermi level can be assigned to the localized 3d states of Fe and Mn. The so-called antibonding e_g and nonbonding t_{2g} states under the O_h symmetry can be identified despite the

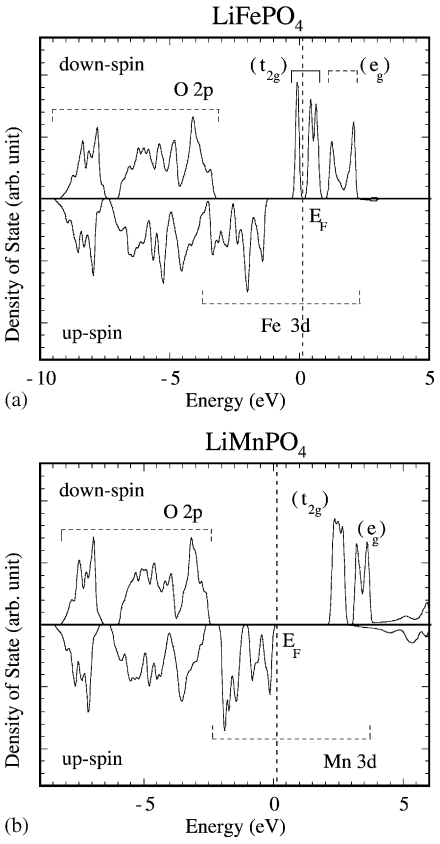

Fig. 1. Total density of states of: (a) $LiFePO_4$; and (b) $LiMnPO_4$. Five 3d states are clearly degenerated by the low symmetry (C_s) around Fe. For convenience, e_g and t_{2g} states under O_h symmetry are denoted. For more details, see [4].

degeneracy induced by the C_s symmetry of the metal site. The DOS clearly shows that the 3d state of metal ions is high spin. We have also performed the calculation for $FePO_4$ and confirmed the high-spin configuration [4]. Fig. 1 also reveals $LiFePO_4$ is a semiconductor with ca. 0.3 eV crystal field band gap and $LiMnPO_4$ is an insulator with ca. 2 eV spin exchange band gap, and this seems the principal reason for the lower electrochemical activity of $LiMnPO_4$ than that of $LiFePO_4$ [1,4]. In addition, it should be mentioned that the two-phase M^{3+}/M^{2+} redox character prohibits to introduce mobile electrons or holes into the bands.

3.2. Comparative study: $(Mn_y^{3+}Fe_{1-y}^{3+})PO_4$ versus $Li(Mn_y^{2+}Fe_{1-y}^{2+})PO_4$ [4]

3.2.1. Unit-cell volume

The variation of unit-cell volume V was calculated using the XRD data and is summarized in Fig. 2 as a function of the Mn content y. The monotonic increase of the unit-cell volume is observed in the series of $Li(Mn_y^{2+}Fe_{1-y}^{2+})PO_4$, while the volume is almost constant in the series of $(Mn_y^{3+}Fe_{1-y}^{3+})PO_4$. This can be explained by the difference of Pauling's ionic radius, i.e. the ionic radius of high-spin Mn^{2+} ($3d^5$, $r = 0.97$ Å) is larger than that of high-spin

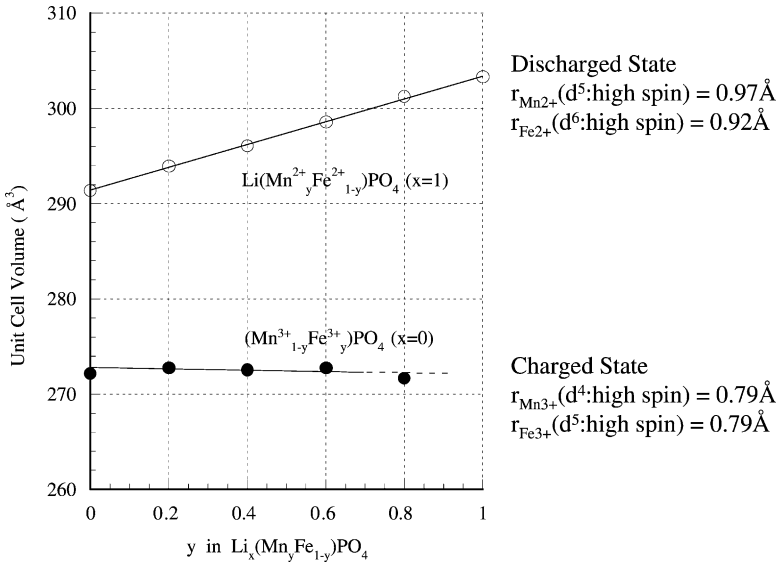

Fig. 2. Change in the unit-cell volume as a function of Mn content y. The data for $(Mn_{0.8}{}^{3+}Fe_{0.2}{}^{3+})PO_4$ is not connected by a solid line because it includes a non-olivine phase, which was observed by Mössbauer spectroscopy but not by X-ray diffraction (Fig. 5) (from [4]).

Fe^{2+} ($3d^6$, $r = 0.92$ Å), whereas high-spin Mn^{3+} ($3d^4$, $r = 0.79$ Å) and high-spin Fe^{3+} ($3d^5$, $r = 0.79$ Å) have almost the same ionic radius, as denoted in Fig. 2.

3.2.2. Jahn-Teller instability by Mn^{3+}

In Fig. 3, the variation of the three lattice constants in the orthorhombic *Pmnb* lattice, *a*, *b*, and *c*, are converted to the expansion percentage. A simple isotropic lattice expansion is confirmed for the series of $Li(Mn_y{}^{2+}Fe_{1-y}{}^{2+})PO_4$ (discharged state) and is linked with the continuous volume increase shown in Fig. 2. Apparently, for the series of $(Mn_y{}^{3+}Fe_{1-y}{}^{3+})PO_4$ (charged state), the elongation of the *a*-axis is compensated for by the shrinkage of the *b*- and *c*-axes, which keeps the unit-cell volume at a constant value independent of the Mn^{3+} content y (Fig. 2). The anisotropic lattice distortion shows a linear increase as a function of Mn^{3+} content y [4].

3.2.3. Local lattice deformation around Mn^{3+}

In phospho-olivines, the edge-shared arrangement of the oxygen-octahedra MO_6 (M = Fe, Mn) as well as the localized character of 3d electrons enhances the selective local lattice distortion around the Jahn-Teller-active Mn^{3+} ions. As shown in Fig. 4, $|F(r)|$ for Fe^{2+} and Fe^{3+} have similar distributions, indicating that the local environment is essentially identical. On the other hand, the amplitude of the Mn^{3+}–O peak in $(Mn_y{}^{3+}Fe_{1-y}{}^{3+})PO_4$ is abnormally low compared to the Mn^{2+}–O peak in $Li(Mn_y{}^{2+}Fe_{1-y}{}^{2+})PO_4$. In general, when the distances between the absorber atom and the coordination atoms are not uniform, the related peak

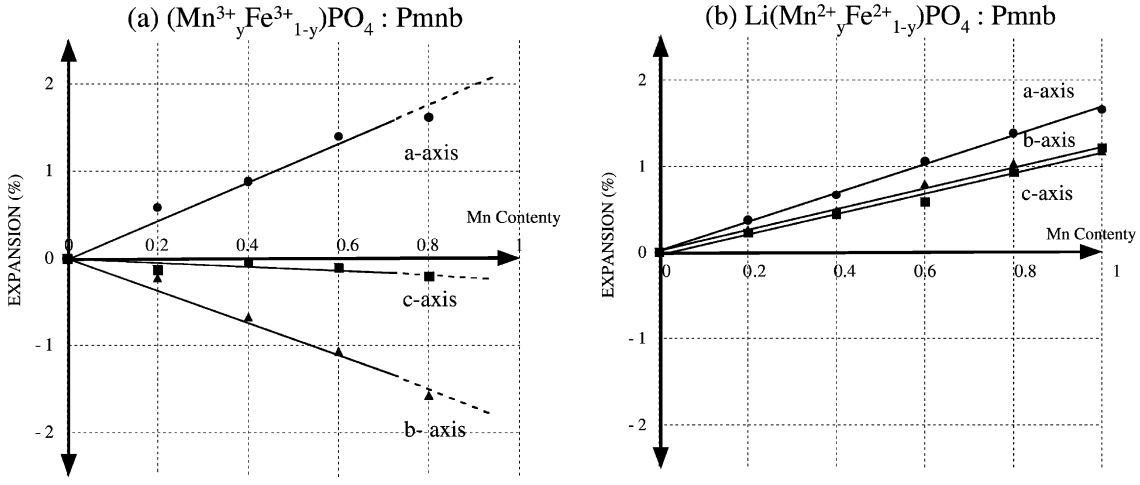

Fig. 3. Unit-cell distortions of the solid solutions: (a) $Li(Mn_y{}^{2+}Fe_{1-y}{}^{2+})PO_4$; and (b) $(Mn_y{}^{3+}Fe_{1-y}{}^{3+})PO_4$. The data for $(Mn_{0.8}{}^{3+}Fe_{0.2}{}^{3+})PO_4$ is not connected by solid line because it includes a non-olivine phase, which was observed by Mössbauer spectroscopy but not by X-ray diffraction (Fig. 5). For more details, see [4].

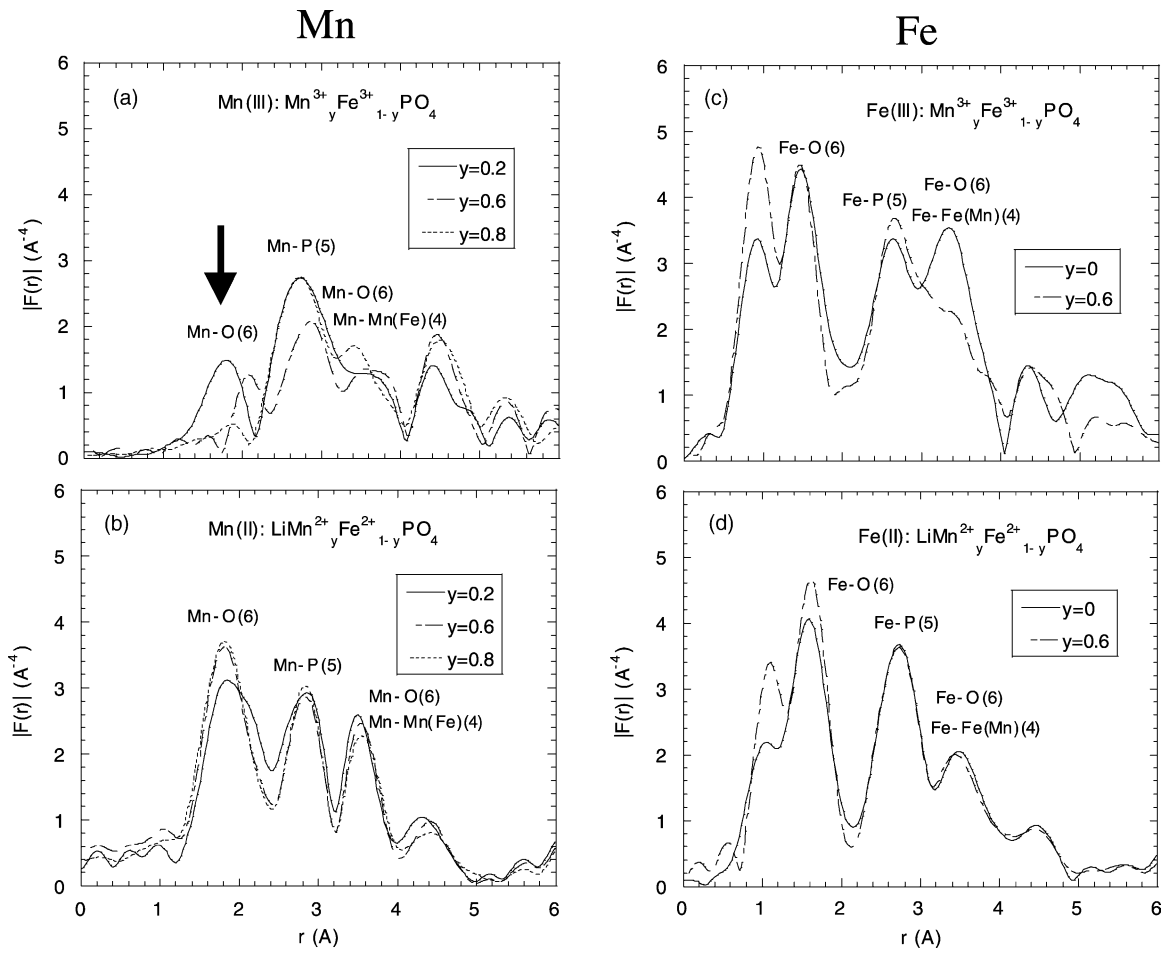

Fig. 4. Fourier transform of the normalized EXAFS χ weighted by k^3 ($k^3\chi$) on the K-edge of: (a) Mn^{3+} in $(Mn_y^{3+}Fe_{1-y}^{3+})PO_4$; (b) Mn^{2+} in $Li(Mn_y^{2+}Fe_{1-y}^{2+})PO_4$; (c) Fe^{3+} in $(Mn_y^{3+}Fe_{1-y}^{3+})PO_4$; and (d) Fe^{2+} in $Li(Mn_y^{2+}Fe_{1-y}^{2+})PO_4$ measured at 300 K. Note that these peaks are at shorter distances than the actual inter-atomic distance, because the phase shift in the electron-scattering process is not considered. For more details, see [6].

shows a broadening and an apparent decrease in the peak height due to interference between the real and imaginary part of the spectrum [35,36]. Consequently, the lattice distortion in Fig. 3 is caused exclusively by the Jahn-Teller effect of Mn^{3+} [37], and the local deformation around the Jahn-Teller-active Mn^{3+} is more severe than the average crystallographic distortion expected from the X-ray diffraction data.

3.2.4. Tolerance limit in $(Mn_y^{3+}Fe_{1-y}^{3+})PO_4$

In the $(Mn_y^{3+}Fe_{1-y}^{3+})PO_4$ system, under the constant volume condition (Fig. 2), the strain energy is accumulated in the lattice and may induce the lattice frustration, which makes the Mn-rich phase ($y = 0.8$) inaccessible and unsuitable for battery application [4]. In addition, larger effective mass of the polaronic electrons around Mn^{3+} would also increase the polarization and promote the inaccessibility [38].

In order to detect the corresponding phase changes quantitatively, Mössbauer spectra were measured for $(Mn_y^{3+}Fe_{1-y}^{3+})PO_4$ with various manganese contents (Fig. 5). Mössbauer measurements were performed because it is very sensitive to minor phases particularly to amorphous phases and/or nanoparticles even at a particle surface [3,4]. Mössbauer spectroscopy is not based on the coherent interaction with the periodic potential of the lattice but involves direct scrutiny of the electronic states around Fe atoms. The quadrupole splitting (QS), which is the gauge for an asymmetric field around the Fe atom, increased from 1.53 to 1.72 mm/s as the Mn^{3+} content y increased. Note the anomaly observed in a sample with manganese content $y = 0.8$. For samples with smaller manganese content $y < 0.6$, no anomaly was observed and the samples are single-phase olivine. The anomaly for $y = 0.8$ was analyzed as another Fe^{3+} doublet (19.3%) with an isomer shift of 0.42 mm/s, which indicates phase separation. This could not be detected by X-ray powder diffraction, in which the amorphous phase or nanoparticles contribute only to the broad background.

Consequently, under the oxidizing condition with NO_2^+/NO_2 redox reaction, the tolerance limit is in the compositional region between 0.6 and 0.8 [4]. For this reason, both in Figs. 2 and 3, the data for the Mn-rich region in $(Mn_y^{3+}Fe_{1-y}^{3+})PO_4$ is not connected by a solid line.

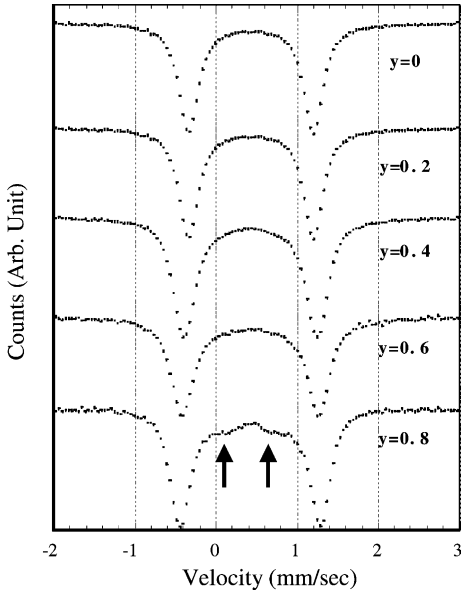

Fig. 5. ^{57}Fe Mössbauer spectra measured for $(Mn_y^{3+}Fe_{1-y}^{3+})PO_4$ (oxidized products of $Li(Mn_y^{2+}Fe_{1-y}^{2+})PO_4$ for 24 h using NO_2BF_4 as oxidizer). Note the anomalies observed for $(Mn_{0.8}Fe_{0.2})PO_4$. For more details, see [4].

3.3. (x, y) Two-dimensional phase diagram for $Li_x(Mn_yFe_{1-y})PO_4$ [6]

The (x, y) two-dimensional phase diagram of the $Li_x(Mn_yFe_{1-y})PO_4$ $(0 \leq x, y \leq 1)$ system [6] given in Fig. 6 establishes some general trends for the phase change. The (x, y) plane can be divided into four regions. It is noteworthy that the Mn^{3+}/Mn^{2+} redox reaction (region of $y \geq x$) proceeds entirely in a two-phase manner; region (b). This can be readily understood by the first-order transition between the Jahn-Teller-active Mn^{3+} phase with cooperative elastic deformation and the Jahn-Teller-inactive Mn^{2+} phase. The lattice frustration exceeding the tolerance limit $(0.6 < y < 0.8)$ induces the inaccessible region (a) for a practical use. Another important aspect is that the single-phase region (c) appears only in Fe^{3+}/Fe^{2+} in a Mn/Fe solid solution system and not in Li_xFePO_4. More detailed analytical results are given in [6].

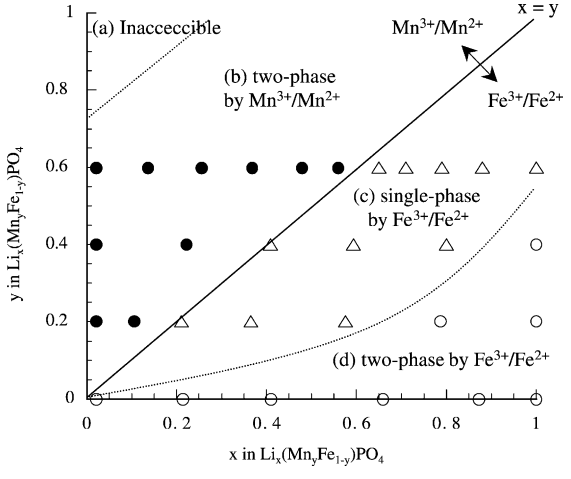

Fig. 6. The (x, y) two-dimensional phase diagram of the $Li_x(Mn_yFe_{1-y})PO_4$ $(0 \leq x, y \leq 1)$ system obtained using X-ray diffraction and Mössbauer spectroscopy. Information is simply given on the single- or two-phase matter together with the valence states of Mn and Fe. The map is divided into four areas: (a) the inaccessible region close to the point $(x, y) = (1, 0)$; (b) the two-phase region by Mn^{3+}/Mn^{2+} (closed circles; $y \geq x$); (d) the two-phase region by Fe^{3+}/Fe^{2+} (open circles; a part of $y \leq x$); and (c) the single-phase region by Fe^{3+}/Fe^{2+} connecting (b) and (d) (open triangles). For more details, see [6].

3.4. Towards efficient cathode performance and production scale-up [3–10]

3.4.1. Choice of the appropriate manganese content

Based on the (x, y) phase diagram discussed in Sections 3.2 and 3.3, primarily $Li(Mn_{0.6}Fe_{0.4})PO_4$ was picked up [5] and its galvanostatic charge/discharge profiles are shown in Fig. 7, together with those of $LiFePO_4$ [3]. The reversible capacity of greater than 160 mAh/g, more than 70% of which is obtained under high-rate ($C/2$) conditions, is almost equal to the theoretical value and cycles very well. Energy density based on the data in Fig. 7 is larger than that of $LiMn_2O_4$ in Wh/l, and surprisingly, larger than that of $LiCoO_2$ in Wh/kg (under the usual charge cut-off at 4.2 V) [3]. They also contributed to the strong tolerance to overcharge/discharge in a cell [11].

Reversible lithium extraction and insertion from and into the sample with $y \geq 0.8$ was possible either chemically or

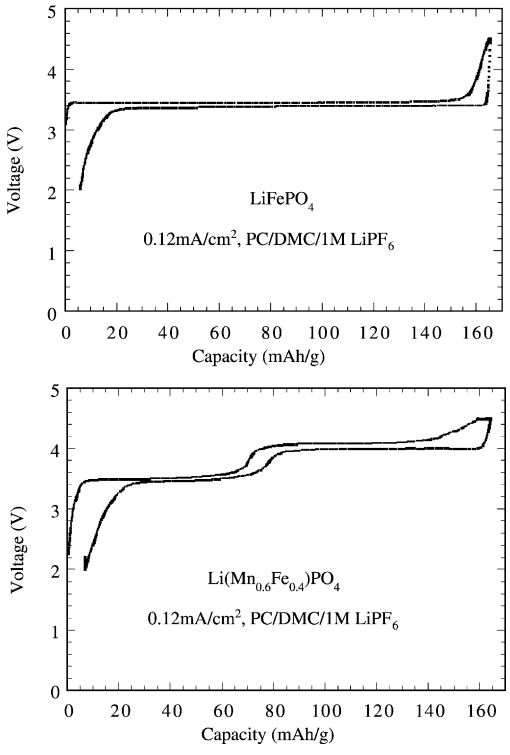

Fig. 7. Charge/discharge profiles measured at room temperature (23 °C) for the optimized electrode composites (90:8:2) of $LiFePO_4$ (top) and $Li(Mn_{0.6}Fe_{0.4})PO_4$ (bottom).

electrochemically, but with smaller capacity and much slower kinetics as speculated from DOS and phase diagram. This observation, coupled with many other intrinsic obstacles, e.g. too low true density of insulating $LiMnPO_4$ (3.4 g/cm^3), led us to the negative strategic decision towards practical application [4,6].

3.4.2. Powder engineering of the electrode composite

The excellent cathode performance as shown in Fig. 7 was achieved with our strategic design consideration of the electrode powder and its composite [3,7–10]. Our original technical solution, which was filed as the primary patents is shown in Fig. 8 [7–10].

Carbon additives to synthetic precursors were first proposed by Ravet et al. [15]. There are three important functions: (1) as a reducing agent to avoid formation of trivalent phases at moderately low sintering temperatures [3]; (2) to block the inter-particle contact and disturb the consequent undesirable particle growth [3]; and (3) to enhance the intra- and inter-particle electronic conductivity [15]. As pointed out by Huang et al. [22], a homogeneous electrode with minimum particle size and intimate carbon contact are required for efficient charge transport. In addition, a dense electrode with a minimum amount of carbon is required for a higher volumetric and gravimetric energy density of the cell [26].

Various kinds of carbon suitable as additives to the electrode composite, were explored for efficient formation of the optimum nanocomposite electrodes satisfying all of the criteria described above. We found that the use of disordered conductive carbons with disordered/graphene (D/G) peak area ratio (1355/1580 cm^{-1}) >0.3 in the Raman spectrum ball-milled with synthetic precursors is most effective [9]. High-energy ball milling is required for ultimate homogeneity and compaction. Thus, the minimum amount of additive carbon for the theoretical capacity was reduced to ca. 3 wt.% with the selected disordered conductive carbon [9].

In addition, the effectiveness of phosphate salts as synthetic precursors must be emphasized [8,10]. Their great

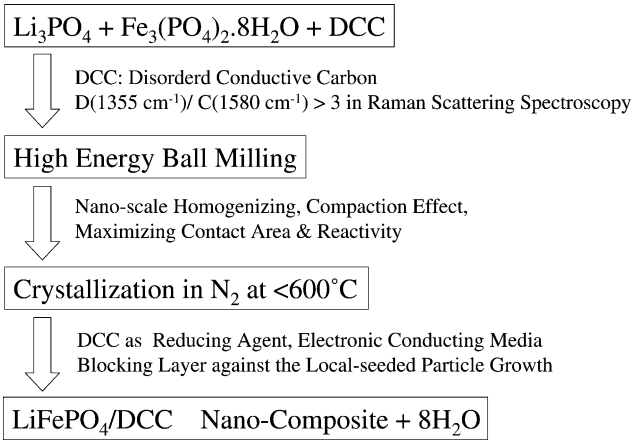

Fig. 8. Sony's original synthetic route for $LiMPO_4$-type cathode composites. For more details, see [7–10].

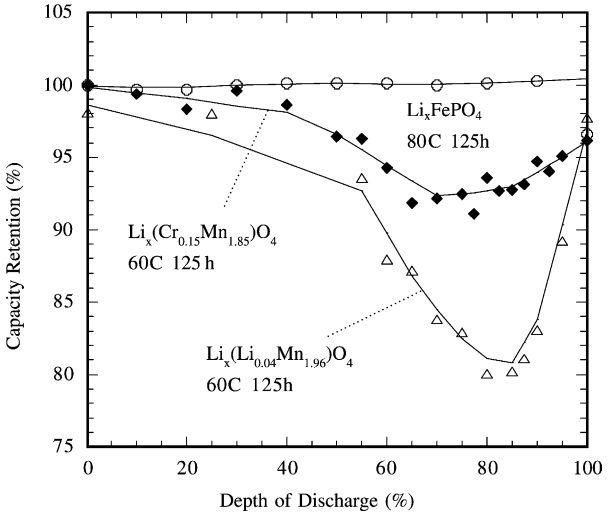

Fig. 9. The capacity retention after the high-temperature storage of coin cells at various depth of discharge, for olivine $LiFePO_4$ (80 °C, 125 h), spinel $Li(Cr_{0.15}Mn_{1.85})O_4$ (60 °C, 125 h), and spinel $Li(Li_{0.04}Mn_{1.96})O_4$ (60 °C, 125 h) (from [7,8]).

advantage is effective sample production (product/input weight ratio, $R = 76.7\%$) without pollutant gas evolution (water being the only exhaust). This makes phosphate salts very suitable for scale-up to mass production. Most of the methods reported so far involve evolution of unfavorable gas such as acetates, ammonia, oxalates, etc., coupled with low R ratios below 50%.

3.5. Stability under unusual conditions [3,7,8]

Many researchers have already pointed out the resistance to combustion of phospho-olivines in the fully charged state [1,3,7,8,25,33]. Here, as another example of the excellent stability of phospho-olivines in actual cells, we demonstrate the capacity retention under the long-term, high-temperature storage up to 80 °C [7,8]. The coin cells after two cycles of charge/discharge processes were exposed to the constant temperature condition at 80 °C for 125 h. The cells were set to the various depths of discharge (DOD) before storage. After storage, the capacity retention (CR) and self-discharge were evaluated, $CR(\%) = 100C_{AS}/C_{BS}$, where C_{AS} and C_{BS} are the discharge capacity within 4.5–3.0 V after and before the storage, respectively. As shown in Fig. 9, CR of Li_x-$FePO_4$ is close to 100% over a wide depth of discharge (DOD in percentage) and self-discharge was negligible even after 125 h storage at 80 °C. This is in contrast to the large capacity loss in the $LiMn_2O_4$-based cathodes even under the lower-temperature (60 °C) storage conditions [39,40].

4. Conclusions

Our first principle calculations revealed $LiFePO_4$ is a semiconductor with ca. 0.3 eV band gap and $LiMnPO_4$ is an insulator with ca. 2 eV band gap, which seems the major

intrinsic obstacle to a facile redox reaction at 4V versus Li/Li^+ in the Mn-rich ($y > 0.8$) phase. In addition, the two-phase M^{3+}/M^{2+} redox character prohibits the introduction of mobile electrons or holes into the bands. The Jahn-Teller deformation around Mn^{3+} has significant influence on the phase diagram of $Li_x(Mn_yFe_{1-y})PO_4$ and also disturbs the smooth reaction. The inherent low conductivity of olivine-type materials can be overcome by the use of a dense nanocomposite formation with disordered conductive carbon, and the use of phosphate-based starting materials facilitates the scale-up of production. This original scientific and engineering works [2–14] performed during the period of 1994–1999, especially on the optimum $C/LiMPO_4$ composite formation (Hosoya's method) [9,10], was transferred to the battery production section at Sony to develop commercial cells, and detailed experimental traces have been followed [34]. Olivine-type $LiFePO_4$ have undoubtedly established their position as the next generation of cathode material for lithium-ion batteries [41]. This is largely due to their extremely stable nature and good energy density [3]. Furthermore, the good news from Chiang and co-workers is that the bulk conductivity enhancement is dramatic (by a factor of 10^8) with a small amount of doping into Li sites to form M^{3+}/M^{2+} mixed valence state [42]. Advanced lithium-ion batteries will be realized in the near future with much better cycle performance, wide-operating temperature, safe operation, strong tolerance to overcharge/discharge, and possibly higher energy density by drastic simplification or removal of the external protective microdevices.

Acknowledgements

The authors would like to thank K. Tanaka for his insightful suggestions at an early stage of this work. K. Ishikawa is gratefully acknowledged for her continuous contribution by the ICP measurements.

References

[1] A.K. Padhi, K.S. Nanjundaswamy, J.B. Goodenough, J. Electrochem. Soc. 144 (1997) 1188.
[2] K. Hinokuma, Patent JP9-171827 (1995).
[3] A. Yamada, S.-C. Chung, K. Hinokuma, J. Electrochem. Soc. 148 (2001) A224.
[4] A. Yamada, S.-C. Chung, J. Electrochem. Soc. 148 (2001) A960.
[5] A. Yamada, Y. Kudo, K.-Y. Liu, J. Electrochem. Soc. 148 (2001) A747.
[6] A. Yamada, Y. Kudo, K.-Y. Liu, J. Electrochem. Soc. 148 (2001) A1153.
[7] A. Yamada, M. Hosoya, S.-C. Chung, K. Hinokuma, Y. Kudo, K.-Y. Liu, in: A. Manthiram, P.N. Kumta, S.K. Sundaram, G. Ceder (Eds.), Materials for Electrochemical Energy Conversion and Storage, American Ceramic Society, Westerville, 2002, pp. 189–204.
[8] A. Yamada, M. Hosoya, S.C. Chung, Y. Kudo, K.Y. Liu, in: G. Nadri, R. Koetz, B. Scrosati, P.A. Moro, E.S. Takeuchi (Eds.), Advanced Batteries and Supercapacitors, PV2001-21, The Electrochemical Society, Pennington, NJ, 2001.
[9] M. Hosoya, K. Takahashi, Y. Fukushima, Patents JP2002-75356, EP1184920, EP1193787, US2002114754 (2002).
[10] M. Hosoya, K. Takahashi, Y. Miyaki, Y. Fukushima, Patents JP2001-250555, EP1193786, EP1193787, US20026061274 (2001).
[11] A. Yamada, T. Yamahira, Patents JP2001-307730, EP1150368, US2002004169 (2001).
[12] A. Yamada, S.-C. Chung, K. Hinokuma, The Electrochemical Society Meeting Abstracts, vol. 2001-1, Washington, DC, 25–30 March 2001 (Abstract no. 51).
[13] A. Yamada, S.-C. Chung, M. Hosoya, G. Li, Y. Kudo, K.-Y. Liu, The Electrochemical Society Meeting Abstracts, vol. 2001-1, Washington, DC, 25–30 March 2001 (Abstract no. 54).
[14] A. Yamada, M. Hosoya, S.-C. Chung, Y. Kudo, K.-Y. Liu, The Electrochemical Society and the International Society of Electrochemistry Meeting Abstracts, vol. 2001-2, San Francisco, CA, 2–7 September 2001 (Abstract no. 205).
[15] N. Ravet, J.B. Goodenough, S. Besner, M. Simoneau, P. Hovington, M. Armand, The Electrochemical Society and the Electrochemical Society of Japan Meeting Abstracts, vol. 99-2, Honolulu, HI, 17–22 October 1999 (Abstract no. 127).
[16] S. Andersson, J.O. Thomas, B. Kalska, L. Haggstrom, Electochem. Solid State Lett. 3 (2000) 66.
[17] S. Andersson, B. Kalska, L. Haggstrom, J.O. Thomas, Solid State Ionics 130 (2000) 41.
[18] K. Amine, H. Yasuda, M. Yamachi, Electochem. Solid State Lett. 3 (2000) 178.
[19] P.P. Prosini, D. Zane, M. Pasquali, Electrochim. Acta 46 (2001) 3517.
[20] O. Moreno, M. Vega, F. Alvarado, J. Jaca, J.M. Amores, M.L. Sanjuan, U. Amador, Chem. Mater. 13 (2001) 1570.
[21] S. Yang, P.Y. Zavalij, M.S. Whittingham, Electrochem. Commun. 3 (2001) 505.
[22] H. Huang, S.-C. Yin, L.F. Nazar, Electrochem. Solid State Lett. 4 (2001) A170.
[23] N. Ravet, Y. Chouinard, J.F. Morgan, S. Besner, M. Gauthier, M. Armand, J. Power Sources 97–98 (2001) 503.
[24] S. Okada, S. Sawa, M. Egashira, J. Yamaki, M. Tabuchi, H. Kageyama, T. Konishi, A. Yoshino, J. Power Sources 97–98 (2001) 430.
[25] D.D. MacNeil, Z. Lu, Z. Chen, J.R. Dahn, J. Power Sources 108 (2002) 8.
[26] Z. Chen, J.R. Dahn, J. Electrochem. Soc. 149 (2002) A1184.
[27] C. Masquelier, P. Reale, C. Wurm, M. Morcrette, L. Dupont, D. Larcher, J. Electrochem. Soc. 149 (2002) A1037.
[28] F. Croce, A.D. Epifanio, J. Hassoun, A. Deptula, T. Olczac, B. Scrosati, Electrochem. Solid State Lett. 5 (2002) A42.
[29] M.C. Tucker, M.M. Doeff, T.J. Richardson, R. Finones, J.A. Reimer, E.J. Cairns, Electrochem. Solid State Lett. 5 (2002) A95.
[30] M.C. Tucker, M.M. Doeff, T.J. Richardson, R. Finones, E.J. Cairns, J.A. Reimer, J. Am. Chem. Soc. 124 (2002) 3832.
[31] S. Yang, Y. Song, P.Y. Zavalij, M.S. Whittingham, Electrochem. Commun. 4 (2002) 239.
[32] P.P. Prosini, M. Lisi, D. Zane, M. Pasquali, Solid State Ionics 148 (2002) 45.
[33] M. Takahashi, S. Tobishima, K. Takei, Y. Sakurai, Solid State Ionics 148 (2002) 283.
[34] G. Li, H. Azuma, M. Tohda, J. Electrochem. Soc. 149 (2002) A743.
[35] I. Nakai, T. Nakagome, Electrochem. Solid State Lett. 1 (1998) 259.
[36] H. Yamaguchi, A. Yamada, H. Uwe, Phys. Rev. B 58 (1998) 8.
[37] R.G.J. Sterns, Mineral. Mag. 35 (1966) 777.
[38] Y. Shimakawa, T. Murata, J. Tabuchi, J. Solid State Chem. 131 (1997) 138.
[39] T. Saito, M. Machida, Y. Yamamoto, M. Nagamine, The Electrochemical Society and the International Society of Electrochemistry Meeting Abstracts, vol. 2001-2, San Francisco, CA, 2–7 September 2001 (Abstract no. 180).
[40] Y. Nishi, J. Power Sources 100 (2001) 101.
[41] J.M. Tarascon, M. Armand, Nature 415 (2002) 359.
[42] S.Y. Chung, J.T. Bloking, Y.M. Chiang, Nat. Mater. 2 (2002) 123.